JOURNAL OF GEOPHYSICAL RESEARCH, VOL. 99, NO. C11, PAGES 22,483–22,490, NOVEMBER 15, 1994

# An ERS 1 synthetic aperture radar image of atmospheric lee waves

P. W. Vachon
Canada Centre for Remote Sensing, Ottawa, Ontario, Canada

O. M. Johannessen and J. A. Johannessen[1]
Nansen Environmental and Remote Sensing Center, Bergen, Norway

**Abstract.** An ERS 1 synthetic aperture radar (SAR) image of the island Hopen shows a distinct 7.6-km wavelength wave phenomenon near the island. This wave phenomenon is interpreted as the surface imprint on open water of atmospheric lee waves. The pattern is visible in the SAR image, since the lee waves modulate the horizontal wind speed near the ocean surface which, in turn, modulates the surface roughness and the radar cross section. The physical setting for the observation is presented and discussed. The lower bound on horizontal wind speed modulation is estimated to range from $3 \pm 2$ ms$^{-1}$ (for the wind speed minima) to $12 \pm 2$ ms$^{-1}$ (for the wind speed maxima) based upon the observed radar cross-section modulation and the ERS 1 scatterometer wind retrieval model CMOD4. The wavelength and wind speed modulation are consistent with linear lee wave model predications. The model uses an atmosphere with an exponential profile of the Scorer parameter (ratio of buoyancy frequency to wind speed) to represent a shallow, ground-based inversion layer observed at Bear Island and a bell-shaped barrier to represent the forcing effects of Hopen.

## Introduction

Wind speed variations at the ocean surface modulate the local surface roughness and, in turn, can be detected using imaging radars. The wind speed variations can be associated with wave phenomena in the atmospheric boundary layer. For example, atmospheric gravity waves have been detected in synthetic aperture radar (SAR) imagery through this mechanism [*Thomson et al.*, 1992]. Gravity waves are internal waves for which gravity is the restoring force. Frequently, they are associated with temperature inversions in the lower troposphere that serve as waveguides. There are many possible generation mechanisms.

Lee waves are a special case of atmospheric gravity waves in which the wave motion is forced over a terrain obstacle (see *Gossard and Hooke* [1975], for example). In the steady state, lee waves are stationary (standing) with respect to the terrain feature, but they are propagating relative to the mean airflow.

Observations of lee waves are rather common in visible remote sensing imagery (see *Gjevik and Marthinson* [1978], for example) in which they appear as wavelike cloud patterns. The spatially periodic uplifting of moist air results in condensation and forms cloud patterns associated with the lee wave crests. *Gjevik and Marthinson* [1978] showed that the wavelength scale and arrangement of wave crests in the lee wave pattern can be predicted using vertical soundings of atmospheric stratification and wind speed.

In this paper we consider an image (Figure 1) from the ERS 1 SAR (C band VV polarization) that appears to show atmospheric lee waves associated with the island Hopen (76.5°N 25.0°E, southeast of Svalbard in the Barents Sea). The data were processed to the low-resolution ERS 1 SAR image product (LRI) (100-m resolution, 75 looks) at the Tromsø satellite station (TSS). The image clearly shows the island surrounded by loosely packed ice floes, with a large ice-free area on the western side that was created by easterly winds that had persisted over the previous 24-hour period. Six well-defined wave crests of 7.6-km wavelength oriented nearly parallel to the island are readily apparent. Two of the six crests are over open water. The ice in the top portion of Figure 1 was composed of large, densely packed floes, while that in the bottom was composed of smaller, loosely packed floes. The open water around the smaller floes provides an imprint of the lee waves on the open water roughness, thus allowing the pattern to

[1]Now at European Space Research and Technology Centre, Noordwijk, Netherlands



Paper number 94JC01392.
0148-0227/94/94JC-01392$05.00

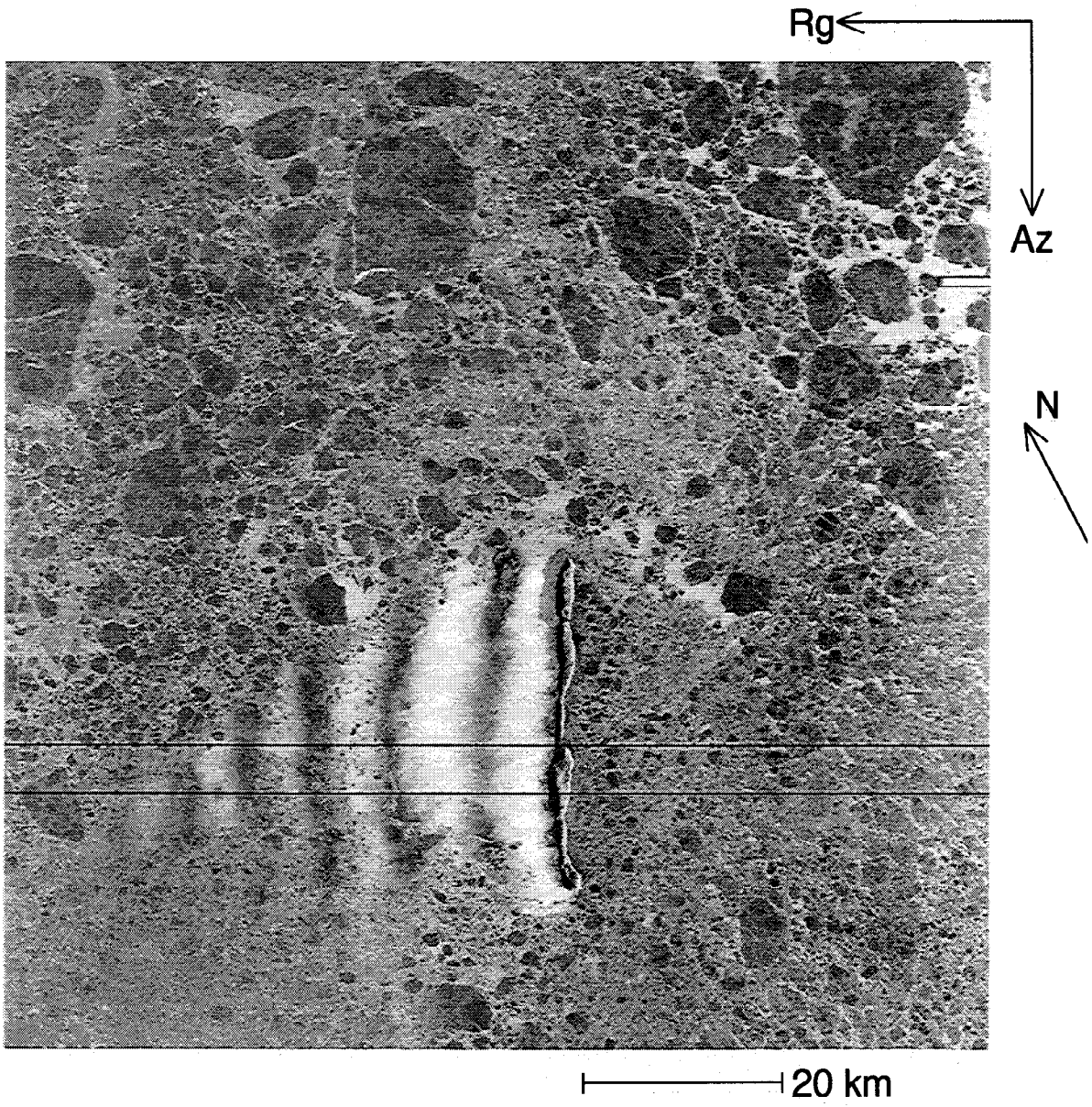


**Figure 1.** ERS 1 synthetic aperture radar (SAR) image (Copyright ESA/Tromsø satellite station 1993) of an atmospheric lee wave associated with Hopen. The image was acquired on June 20, 1993, at 1030 UTC. The image center is near 76.8°N 25.3°E. The horizontal lines indicate the extent of azimuth (Az) averaging carried out to create the radar cross-section profiles shown in Figure 2.

be imaged, even over the ice-covered region. The dense ice in the top portion of the image appears to have constrained the wave pattern to its peculiar wedgelike shape.

As with atmospheric gravity waves observed in SAR images elsewhere [*Thomson et al.*, 1992], these waves are imaged, since they modulate the horizontal wind speed near the ocean surface which, in turn, modulates the surface roughness and the radar cross section. Therefore using radar cross section calibrated SAR image data and a scatterometer wind retrieval model, we can treat the SAR as an imaging scatterometer and estimate the amplitude of these waves, in addition to their wavelength scale, directly from the SAR image. Thus these SAR observations are unique as compared to visible image remote sensing studies of atmospheric lee waves in which only the wavelength scale and the arrangement of the wave crests through the cloud pattern could be analyzed. This use of SAR imagery over the ocean illustrates the potential of calibrated SAR for providing wind vector variations over kilometer scales. This information could be useful in near-shore regions or near the marginal ice zone.

In the next section the physical setting for this observation is reviewed. We also have available radiosonde soundings from Bear Island and the corresponding advanced very high resolution radiometer (AVHRR) visible image. In the following section we consider a linear model for atmospheric lee waves and compare the model results with the observed wave characteristics.

## Observations

### SAR Image and Interpretation

The digital numbers in the SAR image were corrected for range-dependent radar cross-section ($\sigma^\circ$) variations (the elevation antenna pattern, range spreading losscs, and local incidence angle [*Laur*, 1992]) and converted to radar cross section using a calibration constant appropriate for the TSS LRI product [*Malinas et al.*, 1993]. An along-crest-averaged profile of $\sigma^\circ$ was extracted and is plotted as the solid line in Figure 2.

It is well known that the radar cross section over the ocean is strongly dependent upon wind speed and viewing geometry (incidence angle and the look direction with respect to the wind vector) [*Moore and Fung*, 1979; *Long*, 1985]. Extensive empirical work has been carried out on this relationship in the context of ERS 1 scatterometer (C band VV polarization) wind retrieval. This has lead to the CMOD4 wind retrieval model [*Stoffelan and Anderson*, 1993] that is now in operational use within the ERS 1 ground segment. CMOD4 is based on wind analyses from the European Centre for Medium-Range Weather Forecasts (ECMWF) and applies to the open ocean with well-developed waves. (Work is in progress to determine a suitable wind retrieval model for the ERS 1 SAR [*Shuchman et al.*, 1993], but that work is not well developed compared with the ERS 1 scatterometer analysis and will not be considered here.)

For wind speed retrieval from calibrated ERS 1 SAR imagery, we propose use of the CMOD4 model. For large amounts of spatial averaging of radar cross section, to the 50-km resolution scale of the ERS 1 scatterometer, for example, this is quite reasonable. For the smaller resolution scales of interest here the applicability of CMOD4 has not been demonstrated. However, provided that the wind is uniform over the resolution cell, that the radar cross-section estimate is statistically reliable, and that there aren't any other local dominant effects on radar cross section (such as wind gustiness, fetch effects, atmospheric fronts, surfactants, grease ice, or wave/current interaction) that would tend to "average out" over the scatterometer resolution scale, this use of CMOD4 is reasonable. We assume an error estimate of $\pm 2$ m/s (the specification for the ERS 1 scatterometer) in this imaging scatterometer application of the SAR.

Included in Figure 2 are plots of $\sigma^\circ$ for various wind speeds based upon CMOD4, the local incidence angle, and a downwind look direction. These curves represent a lower bound for the wind speed, since any look direction off downwind would result in an interpretation in terms of a higher wind speed. The radar cross section has maxima for upwind and downwind look directions for a particular wind speed. The first two wind speed maxima within the lee wave pattern occur over open water. The lower bounds on wind speed are interpreted as corresponding to $12 \pm 2$ ms$^{-1}$ and $10 \pm 2$ ms$^{-1}$ for the first two wind speed maxima, with an intervening wind speed minimum of $3 \pm 2$ ms$^{-1}$. The subsequent wind speed maxima are over ice, or more properly, their image expression is seen in the open water regions around the loosely packed ice floes. We cannot get an accurate estimate of the wind speed for these maxima using CMOD4 owing to the presence of the ice.

We can check the wind speed upstream of the island

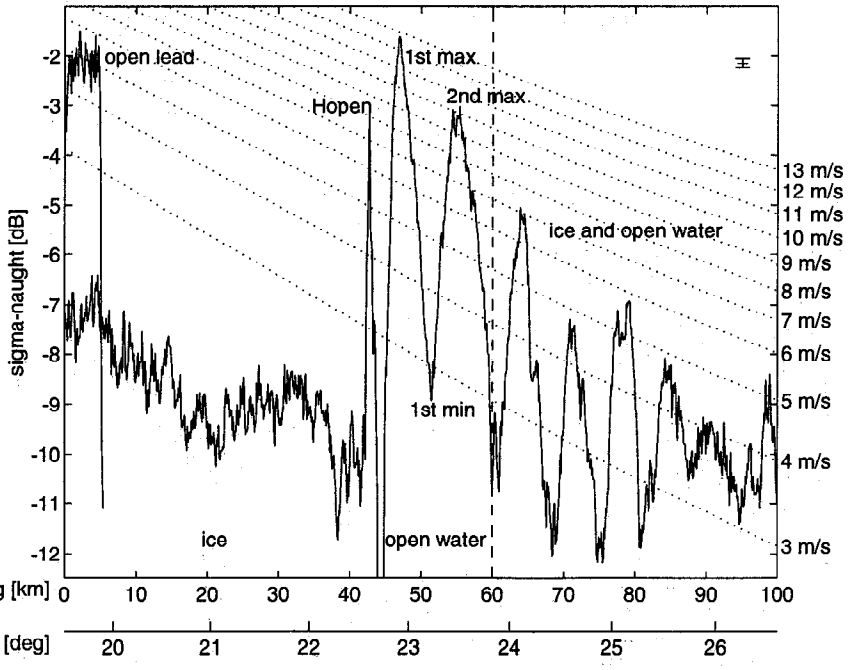


**Figure 2.** Rangeward profiles of radar cross section $\sigma^\circ$ (solid lines) through the lee wave pattern and an upstream open lead with surface wind speed interpretation based upon the ERS 1 scatterometer wind retrieval model CMOD4 (dotted lines). Open water lies between Hopen and the vertical dashed line. The ground range $R_g$ is from the near edge of the scene; $\theta$ is the local incidence angle. The locations of the two profiles are indicated in Figure 1.

by examining the radar cross section in the large open leads near the top right-hand corner of the SAR image. A radar cross-section signature from one such lead is included in Figure 2. The lower bound on the wind speed upstream of Hopen is seen to be $5 \pm 2$ ms$^{-1}$.

### Radiosonde Data

At the time of the ERS 1 pass the surface wind speed measured at Hopen was 7 ms$^{-1}$ from 70°. The nearest upper atmosphere station is on Bear Island, which is approximately 275 km to the southwest. The corresponding Bear Island soundings are shown in Figure 3.

For the sounding the observed temperature $T$ was converted to potential temperature $\theta$ using

$$\theta = T\left(\frac{1000}{p}\right)^{2/7}, \quad (1)$$

where $p$ is the local pressure, and was then differentiated locally to provide the vertical profile of buoyancy frequency $N$

$$N = \sqrt{\frac{g}{\theta}\frac{d\theta}{dz}}, \quad (2)$$

where $g$ is the acceleration due to gravity, and $z$ is the vertical coordinate. The buoyancy frequency provides an indication of local stability. The vertical soundings indicate that there was a shallow inversion layer (increasing temperature, hence, stable stratification) near the surface. The wind speed profile shows an east-southeasterly wind that was more or less perpendicular to the long axis of Hopen.

A problem with this stability analysis is the water vapor content in the lower 2 to 3 km of the atmospheric boundary layer. Technically, this layer is rather less stable than indicated in the buoyancy frequency calculation shown in Figure 3. This has been ignored. On the other hand, Bear Island was surrounded by open water at the time of the sounding. Thus the ice cover around Hopen could have reduced the local water vapor flux, indicating that the buoyancy frequency estimate we have used for Hopen is likely acceptable.

### AVHRR Image

The corresponding NOAA 11 AVHRR visible image is shown in Figure 4. The resolution of this image is about 1 km. This image shows the lee waves but in the cloud pattern, rather than in the effect of surface wind speed. The three observed wave troughs (i.e., regions in which the cloud is absent) correspond to a wavelength scale of about 8 km, which is in agreement with the waves observed in the SAR image. Inspection of the relevant surface analysis chart and the AVHRR image indicates that Hopen and Bear Island were subject to the same basic flow regime and that there were no frontal disturbances present in the area at the time the SAR image and the sounding were acquired. Furthermore, wave phenomena of similar scale can be seen throughout much of the AVHRR image. This justifies utilizing the Bear Island radiosonde data to analyze lee waves near Hopen.

## Lee Wave Model

The literature on lee waves is vast, with significant studies appearing 50 years ago (see *Queney* [1948], for example). The modeling of steady state lee waves usu-

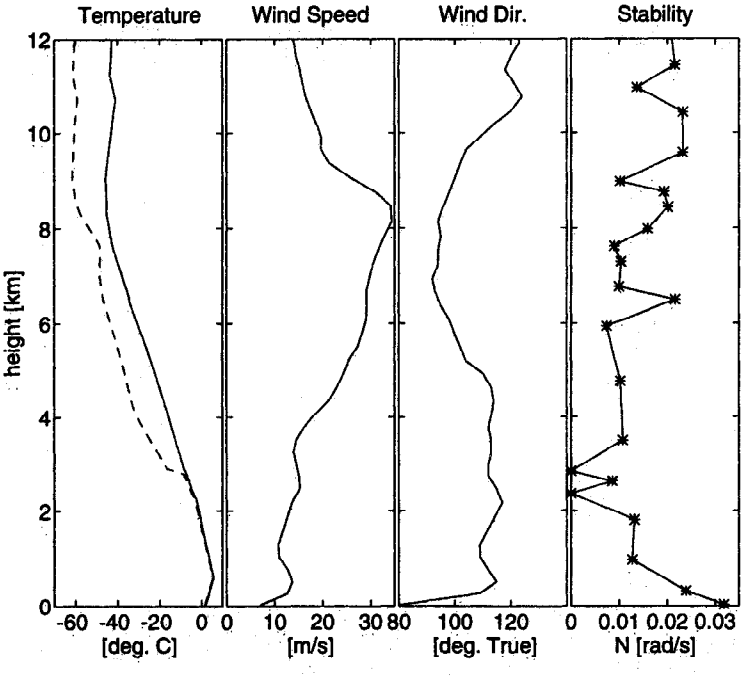


**Figure 3.** Bear Island radiosonde sounding from June 20, 1993, at 1200 UTC. For the temperature plot the solid line is temperature, while the dashed line is dew point temperature. The stability is represented by direct, local computations of the buoyancy frequency $N$.

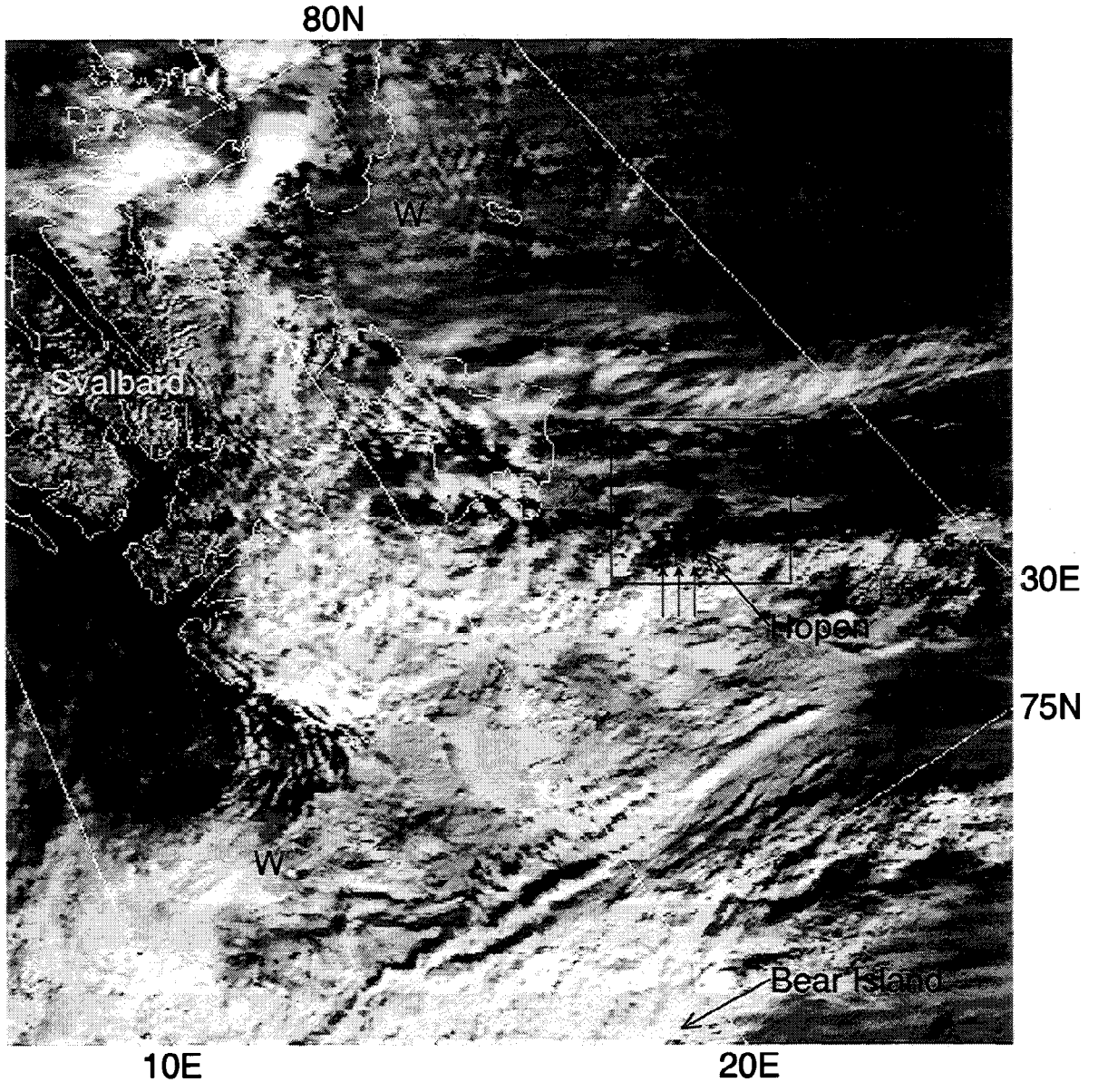


**Figure 4.** NOAA 11 advanced very high resolution radiometer (AVHRR) image of channel 2 reflectance acquired on June 20, 1993 at 1031 UTC. Hopen is located near 76.5°N 25.0°E. The box to the right of image center indicates the approximate extent of the SAR image of Figure 1. Some wavelike disturbances are indicated by "W." The three wave troughs associated with Hopen are indicated by the set of three parallel arrows.

ally starts from linearized equations of motion and determines a solution subject to a sinusoidal lower boundary condition. Generalization to more realistic lower boundaries is carried out by Fourier synthesis. The bell-shaped barrier

$$\zeta(x,0) = \frac{Hb^2}{b^2 + x^2} \quad , \tag{3}$$

where $H$ is the barrier height, $b$ is its half width, and $x$ is the horizontal coordinate, has been successfully used in analytic studies, since its Fourier transform, an exponential function, is particularly simple.

A one-layer atmosphere model with uniform wind speed and buoyancy [*Queney*, 1948] can lead to lee wave disturbances. However, the waves tend to damp quickly downstream and do not predict a strong horizontal wind speed modulation near the ground unless the width of the barrier matches the natural oscillation wavelength. However, a single-layer model is not generally suitable, since the atmosphere often consists of several distinct layers [*Gossard and Hooke*, 1975].

The first useful predictions of lee wave parameters were based upon a a two-layer model [*Scorer*, 1949]. Generalization to three or four layers is possible [*Corby and Sawyer*, 1957], but the added complication does not seem to be necessary when describing low-order lee wave modes in the lower troposphere. In multiple layer models each layer is characterized by a thickness $H_i$, buoy-

ancy frequency $N_i$, and wind speed $U_i$. The natural wavelength scale for gravity waves in each layer is given by the Scorer parameter $k_{N_i} = N_i/U_i$. The boundary conditions between the layers lead to resonant lee wave modes, while the shape of the barrier controls the lee wave amplitude.

Here we will consider a more sophisticated model in which the Scorer parameter is assumed to decay exponentially with height [*Palm and Foldvik*, 1960]. This model has been successfully used in predicting lee wave characteristics (wavelength and vertical velocity) [*Foldvik*, 1962]. Following the methodology proposed by *Foldvik* [1962], we may write

$$k_N(z) = \frac{N(z)}{U(z)} = l_0 \exp\{-cz\} \ , \qquad (4)$$

where $l_0$ and $c$ are constants that may be determined from observed values of $U(z)$ and $N(z)$. We proceed by smoothing the soundings of $U(z)$ and $N(z)$, as shown in Figure 5, and then carrying out a least squares fit of (4) to the ratio of the smoothed profiles. We found that $l_0 = 2.57 \pm 0.03$ km$^{-1}$ and that $c = 0.60 \pm 0.01$ km$^{-1}$ where the error tolerance is based upon the standard error of the least squares fit. The resulting fit is also shown in Figure 5. The exponential fit is seen to be very good in the lower 4 km of the troposphere. The divergence from the exponential fit at higher altitudes does not cause a problem, since we are interested in the lee wave effects in the lower few kilometers of the troposphere. Furthermore, stable layers at higher altitudes are known to have little effect on low-order lee wave solutions near the surface [*Corby and Sawyer*, 1957].

The resonant lee wave modes are determined by solving

$$J_{k_r/c}\left(\frac{l_0}{c}\right) = 0 \ , \qquad (5)$$

where $J_\nu(l)$ is the Bessel function of the first kind of order $\nu$. From this the resonant wavenumber is found to be $k_r = 0.81 \pm 0.03$ km$^{-1}$, which corresponds to a resonant wavelength scale of $L = 7.8 \pm 0.3$ km, which is in good agreement with the wavelength scale observed in the SAR and AVHRR imagery.

General solutions for the vertical velocity perturbation $w(x, z)$ are given by *Palm and Foldvik* [1960]. Assuming continuity in two dimensions, we can directly calculate the vertical streamline deflection $\zeta(x, z)$ from

$$w(x, z) = U(z)\frac{\partial \zeta(x, z)}{\partial x} \ , \qquad (6)$$

where $U(z)$ is the steady state horizontal velocity upstream from the barrier. The corresponding horizontal velocity is given by

$$u(x, z) = -U(z)\frac{\partial \zeta(x, z)}{\partial z} \ . \qquad (7)$$

Hopen has local peaks up to 370 m high and is about 1 km wide and about 33 km long, with its long axis ori-

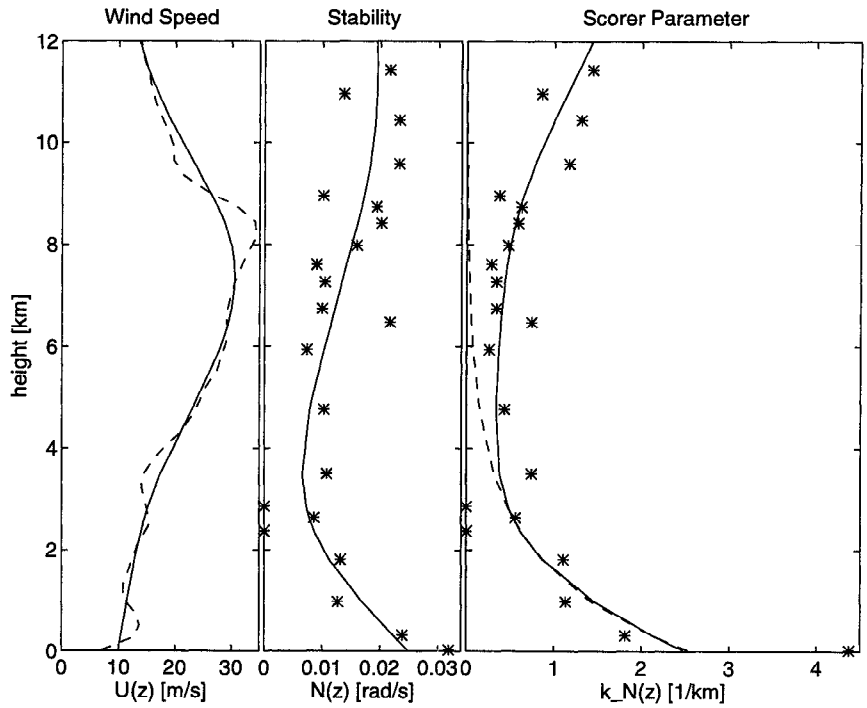


**Figure 5.** Smoothed profiles of wind speed $U(z)$, buoyancy frequency $N(z)$, and Scorer parameter $k_N(z) = N(z)/U(z)$. For the wind speed the dashed line is the observed data. For the stability and the Scorer parameter, the stars are the observed data. In each case the solid line is the smoothed profile. For the Scorer parameter the dashed line is the exponential fit for the lower troposphere.

ented from northeast to southwest. The average height is taken as $H = 200$ m and the half-width as $b = 300$ m. A consequence of the linearized, lower boundary condition is that the lowest level streamline, i.e., the one that touches the ground far upstream from the barrier, tends to pass through the top of the physical barrier being modeled [*Palm and Foldvik*, 1960]. The lowest level streamline represents the actual barrier. We require that this streamline match the height of the physical barrier of interest. In this case we chose a lower boundary condition based upon a barrier height of $H = 320$ m in order to force the lowest level streamline to pass just over the tip of the 200 m physical barrier. The resulting set of streamlines based upon this model and $U(0) = 7$ ms$^{-1}$ is drawn in Figure 6, along with the derived ground level wind speed.

The resonant wave is trapped in the lower troposphere with maximum amplitude near the top of the surface-based inversion layer at about 600 m altitude. The maximum horizontal wind speed at the ground-level is found to be about 11.3 ms$^{-1}$ while the minimum is about 3.5 ms$^{-1}$ which are in good agreement with the lower bound wind speeds deduced from the calibrated SAR image. The amplitude of the resonant portion of the solution for this model (about 3.9 ms$^{-1}$ at ground level in this case) is roughly proportional to the barrier parameters $H$ and $b$ and to the upstream wind speed $U(0)$. The lee wave appears in the local cloud pattern in the regions of uplift (upward deflection of the streamlines). Thus the cloud pattern signature observed in the visible image and the surface wind speed maxima observed in the SAR image are 180° out of phase. The resonant lee wave mode persists as $x$ increases, since there is no damping mechanism in this model. Despite this the model predictions of wavelength and surface wind speed modulation are in reasonable agreement with the SAR-observed lee wave.

## Conclusions

An ERS 1 SAR image of Hopen shows the surface manifestation of well-defined atmospheric lee waves. The pattern is visible, since the horizontal wind speed modulation associated with the lee waves modulates the surface roughness which, in turn, is sensed by the SAR as changes in the local radar cross section. The wavelength of the lee wave is about 7.6 km. On the basis of the CMOD4 scatterometer wind retrieval model and the calibrated SAR image we estimate that the lower bounds on the associated surface wind speed modulation were $12 \pm 2$ ms$^{-1}$ for the wind speed maxima and $3 \pm 2$ ms$^{-1}$ for the wind speed minimum.

The lee wave pattern observed in the SAR image is in agreement with cloud patterns observed in a coincident AVHRR visible image. Also, the wavelength scale and wind speed modulations are consistent with linear lee wave model predictions that used atmospheric stratification based upon radiosonde soundings taken at Bear Island. In particular, we used a model atmosphere with an exponential profile of the Scorer parameter ($k_N(z) = N(z)/U(z)$) to represent a shallow, ground-based inversion layer and a bell-shaped barrier to represent the forcing effects of Hopen. The model configured in this manner predicted a wavelength scale of $7.8 \pm 0.3$ km with surface wind speeds of 11.3 ms$^{-1}$ for the wind speed maxima and 3.5 ms$^{-1}$ for the wind speed minima. It appears that the observed waves are trapped and amplified by the shallow, surface-based inversion layer acting in conjunction with the wind shear aloft.

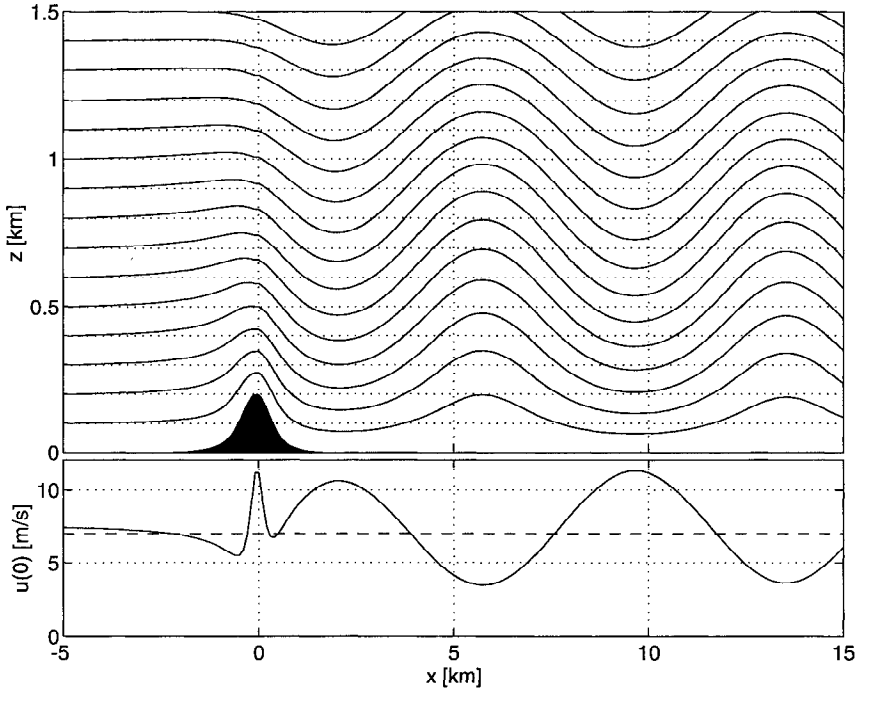


**Figure 6.** A set of streamlines for the linear, one-layer lee wave model of *Palm and Foldvik* [1960] based upon the parameters discussed in the text. The surface wind speed is indicated in the bottom plot.

Extension of the modeling effort to include a multiple-layer atmosphere (especially for the higher regions of the stably stratified troposphere and stratosphere) or nonlinear wave physics is possible, but it does not seem to be necessary in this case.

There are other possible explanations for this observation. For example, it has been suggested to us that this pattern could be the result of a Kelvin-Helmholtz instability of a vortex street created by the wind passing over the island barrier. Another proposal is that this pattern could be the surface signature of rotors associated with gravity waves that are farther aloft. We certainly cannot reject these ideas, and there might be other processes that could explain this observation. However, we are satisfied with the lee wave explanation, especially in light of the demonstrated agreement with the AVHRR image and the lee wave modeling effort.

ERS 1 SAR observations of long-wavelength wave phenomena associated with atmospheric processes over the ocean are common. While we are not claiming to have carried out wind retrieval model validation, this case study does illustrate that a SAR image may be used to measure kilometer-scale wind field fluctuations. This could be a useful application of SAR in near-shore regions or near the marginal ice zone and could provide information on atmospheric boundary layer dynamics. The lee wave image is of analytic interest because the pattern may be assumed to be steady state (standing), the wavelength scale may be measured, and the amplitude may be estimated. Each of these parameters may be verified through a simple lee wave model. The more general case of atmospheric gravity waves is rather more difficult to analyze based upon a single SAR image.

Kilometer-scale wind field fluctuations could confuse the oceanographic interpretation of SAR imagery. Furthermore, they could add a level of ambiguity to wind retrieval algorithms that use long-wavelength energy in SAR imagery as an indication of wind direction. These algorithms assume that long-wavelength coherent structure in the SAR image is due to atmospheric boundary layer rolls [*Shuchman et al.*, 1993]. If the wind field fluctuations are actually due to gravity waves, then the orientation of the long-wavelength energy would be 90° to that expected for boundary layer rolls.

The open water region in the lee of Hopen is of interest. It is possible that the lee waves had a role in opening the lead and then in keeping it ice free. This suggests that perturbations in surface wind stress associated with atmospheric gravity wave phenomena could play a role in ice edge dynamics, such as the generation of local leads where we would expect to find enhanced heat flux.

**Acknowledgments.** This paper was prepared with help from G. Digranes and K. Kloster (NERSC). We thank R. Thomson (IOS) and B. Gjevik (U. Oslo) for helpful discussions. PWV is grateful to A. Foldvik (U. Bergen) and E. Palm (U. Oslo) for help with implementation of their lee wave model. This work was carried out while PWV was visiting the Nansen Environmental and Remote Sensing Center in Bergen, Norway with financial support from a Norwegian Research Council research fellowship and CCRS.

## References

Corby, G. A., and J. S. Sawyer, The air flow over a ridge—The effects of the upper boundary layer and high-level conditions, *Q. J. R. Meteorol. Soc., 84*, 25–37, 1957.

Foldvik, A., Two dimensional mountain waves—A method for the rapid computation of lee wavelengths and vertical velocities, *Q. J. R. Meteorol. Soc., 88*, 271–285, 1962.

Gjevik, B., and T. Marthinson, Three-dimensional lee-wave pattern, *Q. J. R. Meteorol. Soc., 104*, 947–957, 1978.

Gossard, E. E., and W. H. Hooke, *Waves in the Atmosphere*, Elsevier, New York, 1975.

Laur, H., Derivation of backscattering coefficient $\sigma^\circ$ in ERS-1.SAR.PRI products, *Tech. Rep. ESA/ESRIN*, Eur. Space Agency, Frascati, Italy, 1992.

Long, A. E., Towards a C-band radar sea echo model for the ERS 1 scatterometer, in Proceedings of 3rd International Colloquium on Spectral Signatures of Objects in Remote Sensing, *Eur. Space Agency Spec. Publ., ESA SP-247*, 29–34, 1985.

Malinas, N. P., R. A. Shuchman, and K. Kloster, Tromsø ERS-1 Calibration, in Proceedings of 2nd Scandinavian SAR Symposium, 28–30 September 1992, Bergen, Norway, *Conf. Rep. 4*, pp. 118–124, Nansen Environ. and Remote Sens. Cent., Bergen, Norway, 1993.

Moore, R. K., and A. K. Fung, Radar determination of winds at sea, *Proc. IEEE, 67*, 1504–1521, 1979.

Palm, E., and A. Foldvik, Contribution to the theory of two-dimensional mountain waves, *Geophys. Norv., XXI* (6), 1–30, 1960.

Queney, P., The problem of air flow over mountains: A summary of theoretical studies, *Q. J. R. Meteorol. Soc., 29*, 16–26, 1948.

Scorer, R. S., Theory of waves in the lee of mountains, *Q. J. R. Meteorol. Soc., 75*, 41–56, 1949.

Shuchman, R. A., J. A. Johannessen, C. Rufenach, K. Davidson, and C. Wackerman, Determination of wind speed, wind direction and atmospheric structure using ERS-1 SAR data during NORCSEX'91, in Proccedings of 1993 International Geoscience and Remote Sensing Symposium (IGARSS'93), *Publ. 93CH3294-6*, pp. 537–539, Inst. of Elec. and Electron. Eng. New York, 1993.

Stoffelan, A., and D. L. T. Anderson, ERS-1 scatterometer data characteristics and wind retrieval skill, in Proceedings of 1st ERS 1 Symposium—Space at the Service of our Environment, *Eur. Space Agency Spec. Publ., ESA SP-359*, 41–47, 1993.

Thomson, R. E., P. W. Vachon, and G. A. Borstad, Airborne synthetic aperture radar imagery of atmospheric gravity waves, *J. Geophys. Res., 97*, 14,249–14,257, 1992.

J. A. Johannessen, ESA/ESTEC, Postbus 299, Keplerlaan 1, 2200 AG Noordwijk, Netherlands.

O. M. Johannessen, Nansen Environmental and Remote Sensing Center, Edvard Griegsvei 3a, N-5037 Bergen, Norway.

P. W. Vachon, Canada Centre for Remote Sensing, 588 Booth Street, Ottawa, Ontario K1A 0Y7 Canada.

(Received December 13, 1993; revised May 6, 1994; accepted May 17, 1994.)